RESEARCH ARTICLE SUMMARY

CELL BIOLOGY

Actin organizes chromosomes and microtubules to ensure mitotic fidelity in the preimplantation embryo

Blake Hernandez, Piotr Tetlak, Ana Domingo-Muelas, Hiroki Akizawa, Robin M. Skory, Goli Ardestani, Mate Biro, Xiaolei Liu, Stephanie Bissiere, Denny Sakkas, Nicolas Plachta*

Full article and list of author affiliations: https://doi.org/10.1126/science.ads1234

INTRODUCTION: During preimplantation development, a single copy of the genome must be propagated through numerous rounds of mitotic cell division. Mitotic errors, if uncorrected, frequently result in chromosome missegregation and aneuploidy, a condition defined by abnormal chromosome number. Aneuploidy represents a major source of congenital defects. Therefore, elucidating the complete set of mechanisms required for mitotic fidelity has remained a longstanding goal of developmental cell biology.

RATIONALE: The classical view of mitotic cell division is that the spindle apparatus maintains principal control of chromosome organization. This control is established following nuclear envelope breakdown, when chromosomes are released from the nucleus, and spindle microtubules must quickly form attachments with kinetochores and chromosome-associated motors. However, the early mouse embryo does not possess centrosomes, the organelles responsible for fast and efficient spindle assembly. Therefore, the acentrosomal spindles of early mouse embryos are initially highly disordered, and proper spindle morphology is not achieved until many minutes after nuclear envelope breakdown. Although this fact has been appreciated for over a decade, the field has struggled to resolve the paradox of compromised spindle assembly during a highly consequential developmental period. A growing body of evidence has suggested numerous roles for the actin cytoskeleton in mitotic cell division. However, this notion challenges the microtubule-centric view of mitosis and has been treated with some skepticism, largely owing to the difficulty of visualizing sparse populations of cytoplasmic actin filaments. We thus set out to reevaluate the paradigm of mitosis and examine the roles of actin filaments in achieving faithful segregation of the genetic material.

RESULTS: By using high-resolution imaging, we resolved a network of actin filaments in the nucleus of early mouse embryos. This network establishes physical interactions with prophase chromosomes through myosin-10, an actin motor localized on mitotic chromatin. Following nuclear envelope breakdown, the network contracts and gathers chromosomes towards the cell center. Notably, network contraction occurs in a motor-independent manner. Rather than relying on nonmuscle myosin II, contractile stress is generated by filament disassembly. We also found the diffusible cross-linker anillin to be essential for network contraction. This mechanism of chromosome organization during the early phases of mitosis is microtubule-independent and occurs before the mitotic spindle is assembled. Disruptions of actin-based chromosome positioning resulted in increased rates of chromosome missegregation. Furthermore, we observed an additional network of actin filaments, which encloses the metaphase spindle. This network is composed of branched actin filaments nucleated by the Arp2/3 complex. We found that perispindle actin prevents uncontrolled spindle elongation, likely by serving as a physical barrier with inhibits microtubule elongation.

CONCLUSION: Our investigation of unconventional mitotic mechanisms reveals that the actin cytoskeleton organizes chromosomes and microtubules during early embryonic development. We identified two distinct actin assemblies which perform functions typically mediated by the centrosome, highlighting the robustness of the developmental process. These findings provide an explanation as to how the early mouse embryo achieves faithful chromosome segregation, despite lacking the canonical set of mitotic machinery. □

*Corresponding author. Email: nicolas.plachta@pennmedicine.upenn.edu Cite this article as B. Hernandez *et al.*, *Science* **388**, eads1234 (2025). DOI: 10.1126/science.ads1234

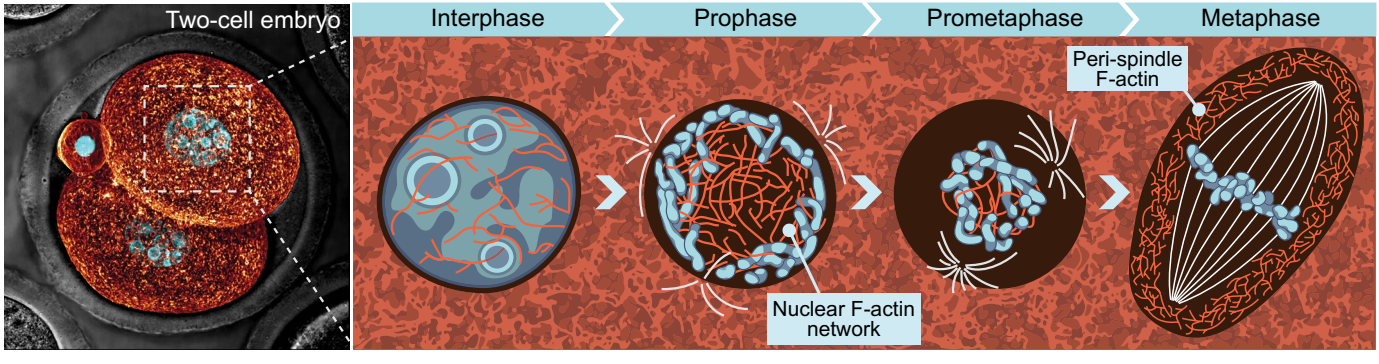

Actin filaments organize chromosomes and microtubules. In the early mouse embryo, nuclear actin filaments establish a dense interconnected network, physically coupled with prophase chromosomes. Following nuclear envelope breakdown, the network contracts and gathers chromosomes near the cell center. Subsequently, an additional network of branched actin filaments encloses the metaphase spindle and prevents its uncontrolled elongation.

CELL BIOLOGY

Actin organizes chromosomes and microtubules to ensure mitotic fidelity in the preimplantation embryo

Blake Hernandez[1,2], Piotr Tetlak[1], Ana Domingo-Muelas[1], Hiroki Akizawa[1], Robin M. Skory[1,3], Goli Ardestani[4], Mate Biro[5,6], Xiaolei Liu[7], Stephanie Bissiere[1], Denny Sakkas[4], Nicolas Plachta[1]*

Following fertilization, the preimplantation embryo undergoes successive rounds of cell division and must accurately propagate the genetic material to ensure successful development. However, early mammalian embryos lack efficient spindle assembly mechanisms, and it remains unclear how error-free chromosome segregation is achieved. In this work, we imaged early mouse embryos and identified a network of nuclear actin cables that organize prophase chromosomes at the nuclear periphery. Following nuclear envelope breakdown, the network contracts and gathers chromosomes toward the cell center. Network contraction was driven by filament disassembly in a myosin II–independent manner. Additionally, we identified a network of branched actin filaments that attenuates metaphase spindle elongation. We also visualized nuclear actin in human embryos, suggesting a conserved role for actin in ensuring mitotic fidelity during early mammalian development.

Successful preimplantation development relies on the error-free propagation of genetic information during each cell division. Abnormal chromosome number, a condition known as aneuploidy, represents a major cause of developmental defects and infertility (*1*). However, the mechanisms that ensure accurate chromosome segregation in the early mammalian embryo remain largely unidentified. The spindle apparatus is the principal structure driving chromosome congression and segregation during mitosis (*2*–*4*). Canonically, centrosomes located at the two spindle poles nucleate microtubules which capture chromosomes following nuclear envelope breakdown (NEBD) (*4*). However, the mouse zygote does not inherit centrioles, which are the primary centrosomal component (*5*–*9*). The first cell divisions of mouse embryogenesis thus occur in the absence of centrosomes. Although the human zygote inherits sperm-derived centrioles during fertilization, the ensuing chromosome segregations are frequently multipolar (*10*), suggesting that centrosomes in the early human embryo are not fully operational. This lack of functional mitotic machinery is at odds with the need to accurately propagate genetic material during development. It thus remains an open question whether microtubule-independent mechanisms play a role in ensuring mitotic fidelity in the early mammalian embryo.

[1]Department of Cell and Developmental Biology, Institute for Regenerative Medicine, Perelman School of Medicine, University of Pennsylvania, Philadelphia, PA, USA. [2]Department of Bioengineering, University of Pennsylvania, Philadelphia, PA, USA. [3]Department of Obstetrics and Gynecology, Division of Reproductive Endocrinology and Infertility, Perelman School of Medicine, University of Pennsylvania, Philadelphia, PA, USA. [4]Boston IVF - IVIRMA Global Research Alliance, Waltham, MA, USA. [5]Garvan Institute of Medical Research, Cancer Ecosystems Program, Darlinghurst, NSW, Australia. [6]EMBL Australia, Single Molecule Science Node, School of Biomedical Sciences, The University of New South Wales, Sydney, NSW, Australia. [7]Department of Medicine, Division of Hematology-Oncology, Perelman School of Medicine, University of Pennsylvania, Philadelphia, PA, USA. ***Corresponding author. Email: nicolas.plachta@pennmedicine.upenn.edu**

Previous studies have exposed diverse roles for filamentous actin (F-actin) during cell division. In mouse oocytes, cortical and cytoplasmic actin assemblies facilitate asymmetric spindle positioning (*11*–*17*). In starfish, porcine, and human oocytes, actin filaments mediate chromosome congression following NEBD (*18*–*20*). Actin filaments also permeate the metaphase spindle in mouse and human oocytes (*21*, *22*). Furthermore, F-actin has been observed within the spindles of nonmammalian organisms, such as *Xenopus laevis* (*23*, *24*). Despite this body of work (*25*), the role of F-actin in mitotic chromosome segregation during early mammalian development remains debated (*26*–*28*).

Visualization of a contractile nuclear F-actin network in the early embryo

To explore the role of F-actin during the first mitotic divisions of preimplantation development we first visualized actin filaments in phalloidin-labeled two-cell mouse embryos, as this is the first stage when both parental genomes are contained within the same nuclear compartment. During interphase, blastomeres displayed high fluorescence intensity at the cortex, and a relatively disordered actin meshwork homogenously distributed throughout the cytoplasm (fig. S1A). We also detected a network of actin cables within the nucleus, spanning the entire nuclear diameter (Fig. 1, A and B). Furthermore, nuclear actin density increased during prophase (Fig. 1, B and C, and fig. S1, E and F). Imaging preimplantation human embryos revealed a similar organization of interphase and prophase nuclear actin cables (Fig. 1, C to E).

In cells containing centrosomes, bipolar spindle assembly is typically achieved during early prometaphase (*29*). By contrast, the early prometaphase spindle of two-cell mouse blastomeres is highly multipolar, and bipolar spindle morphology is not established until late prometaphase (Fig. 1F) (*30*, *31*). This sharp contrast in prometaphase spindle assembly suggests that the mechanisms governing mitotic chromosome organization in the mouse embryo differ from that of centrosomal cell types. We therefore reasoned that a microtubule-independent mechanism may dictate chromosome arrangement during the initial stages of prometaphase.

To evaluate the organization of mitotic chromosomes, we imaged live mouse embryos labeled with SPY650-DNA. During prophase, chromosomes were positioned at the nuclear periphery (Fig. 1G). However, following NEBD, chromosomes and their centromeres rapidly repositioned toward the cell center in a relatively isotropic manner (Fig. 1G; fig. S1, G and H; and movie S1). This centripetal chromosome movement was typically completed within 5 min, characterized by a reduction in the chromosomal scattering volume (Fig. 1, G and H, and fig. S1I). Subsequently, the scattering volume increased moderately as chromosomes aligned at the metaphase plate (Figs. 1, G and H), consistent with previous observations (*27*). Microtubule depolymerization with nocodazole impaired chromosome alignment at the metaphase plate (Fig. 1G) but did not impact the peripheral organization of prophase chromosomes or their centripetal movement following NEBD (Fig. 1, H to J, and fig. S1J). Together with previous work (*27*), these results suggest that prometaphase chromosome dynamics in the early embryo can be divided into two distinct phases: First, following NEBD, chromosomes move centripetally in a microtubule-independent manner; subsequently, microtubules finalize the alignment of chromosomes at the metaphase plate.

We next evaluated the role of nuclear actin cables in the first phase of mitotic chromosome positioning. To image F-actin and chromosomes in live embryos, we microinjected two-cell blastomeres with mRNA encoding the green fluorescent protein (GFP)–tagged Calponin Homology domain of Utrophin [UtrCH-GFP (*32*)] and red fluorescent protein (RFP)–tagged histone 2B (H2B-mRFP1). Imaging the nucleus and spindle regions with <5-s temporal resolution confirmed the presence of a nuclear F-actin network closely associated with prophase

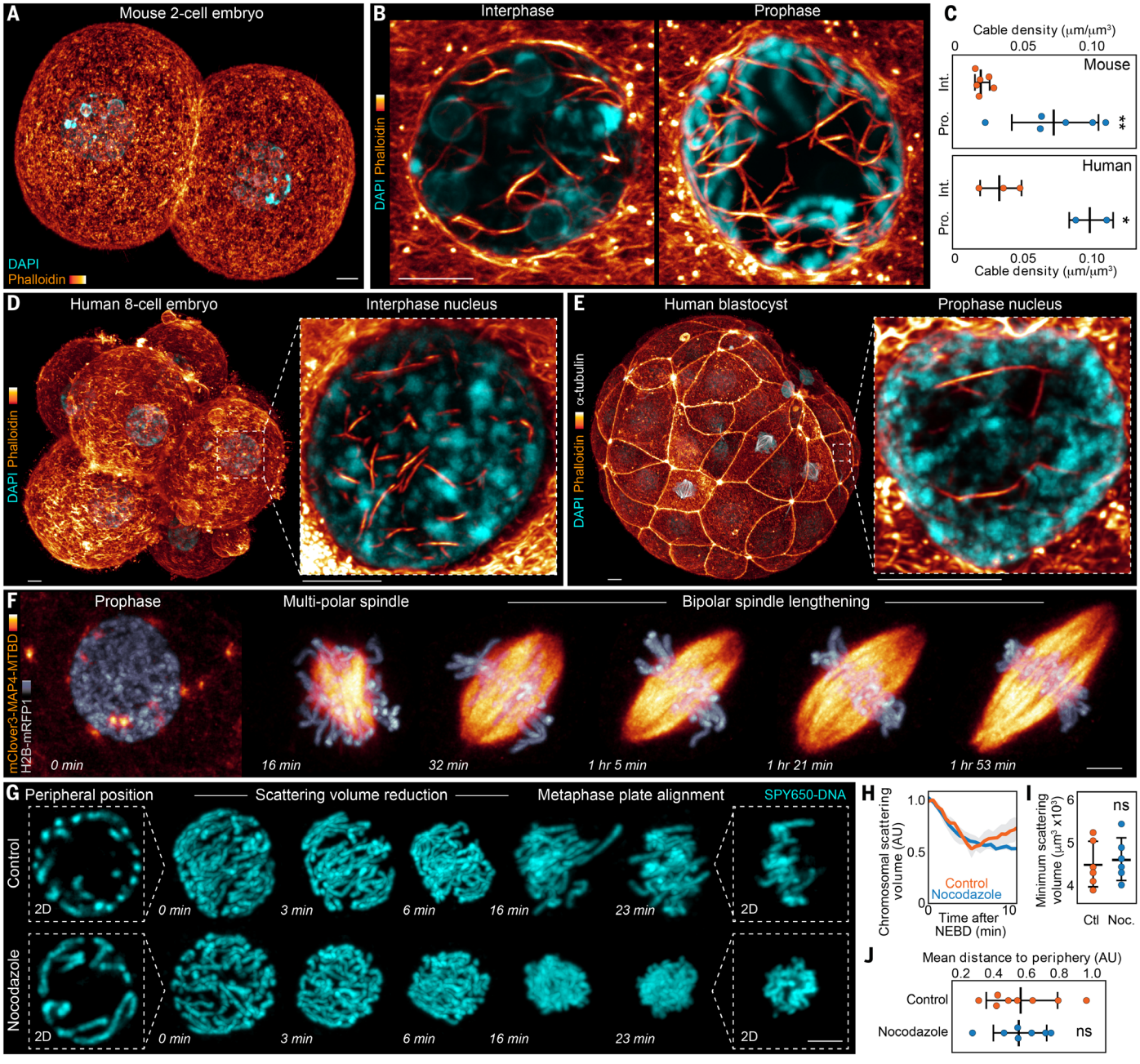

Fig. 1. Identification of nuclear actin cables in the early mammalian embryo. (**A**) Two-cell mouse embryo labeled with DAPI and Phalloidin-Alexa Fluor 488. (**B**) F-actin cables in interphase and prophase nuclei. (**C**) Quantification of actin cable density. Int., interphase; Pro., prophase. (**D** and **E**) Interphase (D) and prophase (E) nuclear actin cables in human embryos. (**F**) Visualization of acentrosomal spindle assembly in the two-cell mouse embryo. Note how spindle microtubules are largely disorganized during early prometaphase. (**G**) Live imaging of chromosomes (SPY650-DNA), illustrating chromosome organization in control and nocodazole-treated embryos. (**H**) Mean chromosomal scattering volume plotted over time. Gray shading represents standard deviation. AU, arbitrary units. (**I**) Quantification of minimum chromosomal scattering volume. (**J**) Quantification of the mean distance of prophase chromosomes to the nuclear periphery. Scale bars, 5 μm [(A), (B), (D), (F), and (G)] and 3 μm (E). $n = 6$ mouse embryos per group [(C), (H), (I), and (J)], three interphase eight-cell human nuclei, and two prophase blastocyst nuclei (C). Two-tailed unpaired t test; $^{*}P < 0.05$; $^{**}P < 0.01$; ns, not significant.

chromosomes (Fig. 2A). Following NEBD, the network contracted, coinciding with centripetal chromosome movement (Fig. 2A and movie S2). Kymograph analysis verified the comotility of actin cables and mitotic chromosomes (Fig. 2B), suggesting a physical coupling (Fig. 2C). During network contraction, nuclear F-actin displayed prominent puncta of high intensity, resembling nodes in a cross-linked network (Fig. 2D). We used these nodes as landmarks to track the position and area of the network over time (fig. S1K). Particle tracking of node coordinates revealed that the network contracts toward the cell center (Fig. 2E and movie S3), indicating that the network is not passively anchored to the cortex, as previously observed in starfish oocytes (*33*). We also observed a gradual decrease in network area following NEBD, further suggesting that the network is under contractile stress (Fig. 2F and movie S4).

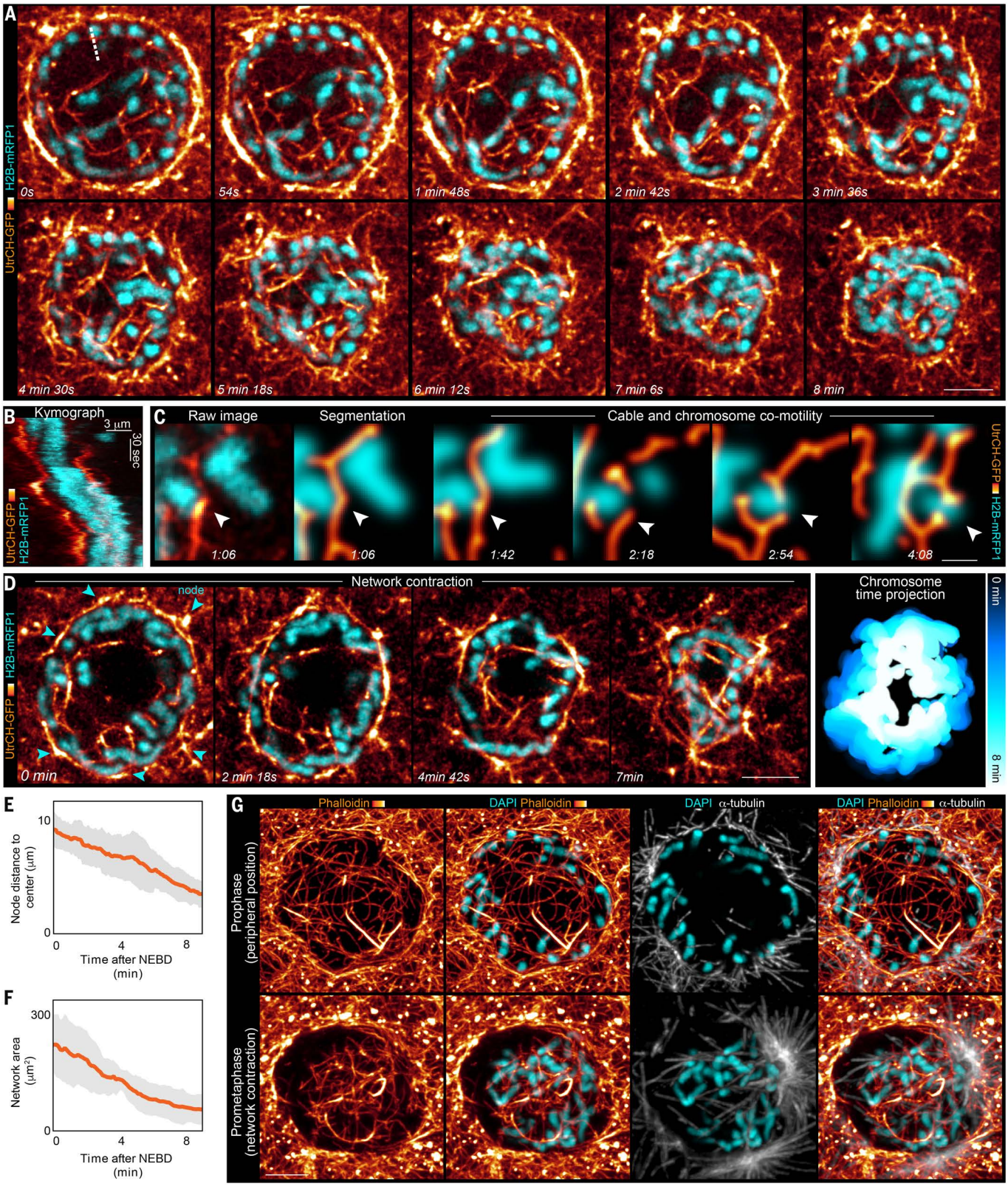

Fig. 2. Visualization of a contractile nuclear actin network. (**A**) Live imaging of network contraction following NEBD. Embryos are expressing UtrCH-GFP and H2B-mRFP1. (**B**) Kymograph illustrating comotility between actin cables and chromosomes during contraction. Kymograph path corresponds to the dashed line shown in (A). (**C**) High-magnification frames from (D) highlighting the comotility of actin cables and chromosomes. Arrow indicates points of actin-chromosome coupling. (**D**) Visualization of F-actin and chromosomes during network contraction. Arrows indicate puncta used as positional landmarks. Time projection shows H2B-mRFP1 signal over network contraction (right). (**E**) Mean distance of network nodes to the nucleus center plotted over time. (**F**) Mean network area (convex hull area) plotted over time. (**G**) Images of fixed embryos illustrating F-actin permeating the nuclear region prior to microtubule infiltration. Scale bars, 5 µm [(A), (D), and (G)], 3 µm (B), and 1 µm (C). $n = 5$ embryos [(E) and (F)].

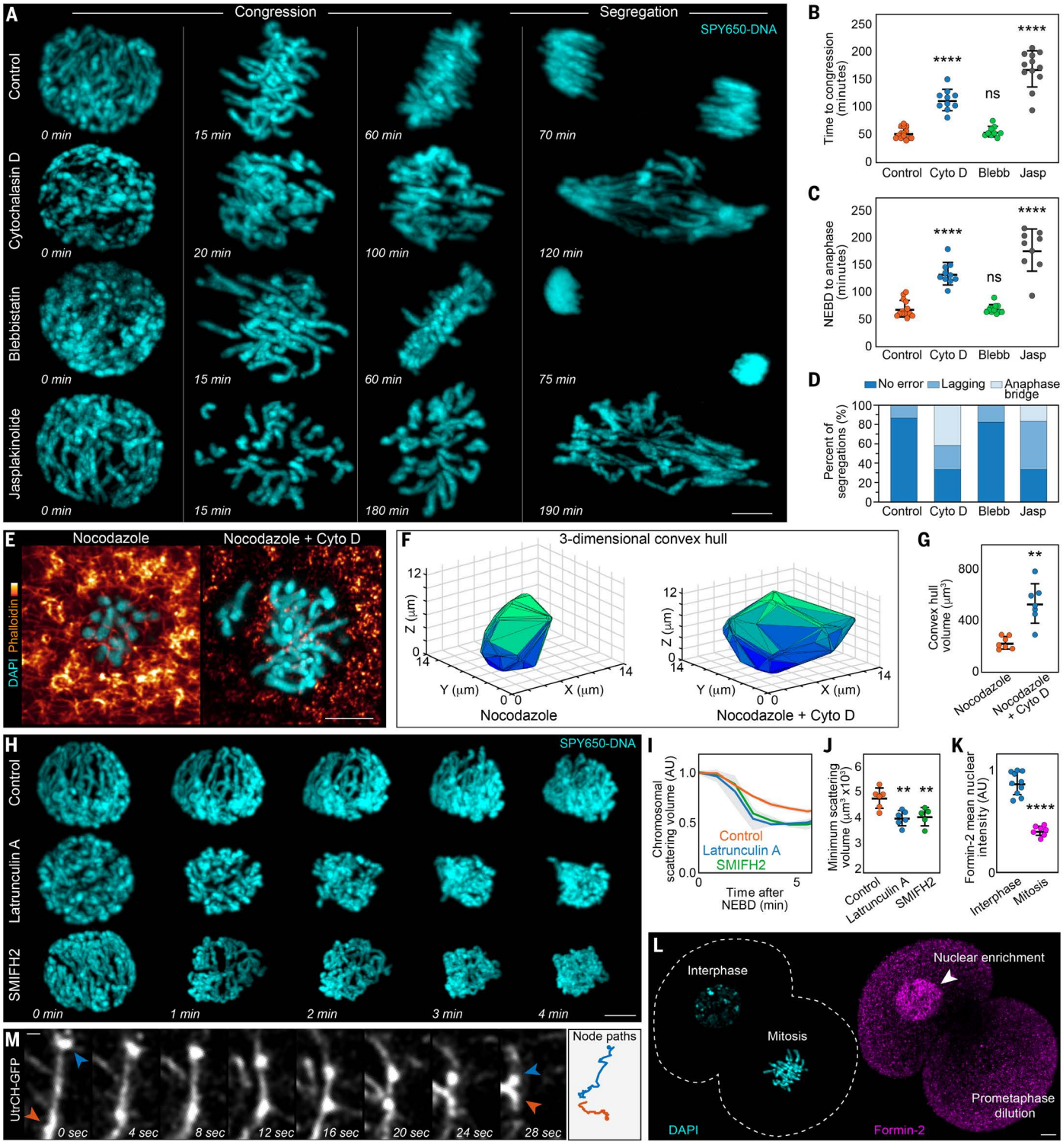

Fig. 3. F-actin depolymerization drives network contraction. (**A**) Live imaging of chromosome congression and segregation in embryos labeled with SPY650-DNA and treated with DMSO (control), cytochalasin D, blebbistatin, or jasplakinolide. (**B**) Quantification of time to chromosome congression. (**C**) Quantification of mitotic duration (NEBD to anaphase). (**D**) Quantification of chromosome segregation errors. (**E**) Visualization of chromosomal scattering in prometaphase-arrested embryos. (**F**) 3D convex hull surface plots generated from processed DAPI signal. (**G**) Quantification of convex hull volume (scattering volume). (**H**) Live imaging of centripetal chromosome movement in embryos treated with DMSO (control), Latrunculin A, or SMIFH2. (**I**) Chromosomal scattering volume plotted over time. (**J**) Quantification of the minimum chromosomal scattering volume. (**K**) Quantification of formin-2 levels during interphase and prometaphase. (**L**) Interphase (left) and prometaphase (right) cells within the same two-cell mouse embryo immunostained for formin-2. Note the nuclear enrichment of formin-2 during interphase and dilution in mitosis. (**M**) Live imaging of actin cable shortening during network contraction. Arrows show cable ends. Scale bars, 5 μm [(A), (E), (H), and (L)] and 1 μm (M). Sample sizes (embryos): 14 control, 10 Cyto D, 9 Blebbistatin, 12 Jasplakinolide [(B) to (D)]; 7 Nocodazole, 7 Nocodazole + Cyto D (G); 6 control, 6 Latrunculin A, 5 SMIFH2 (I and J); 10 interphase, 7 mitosis (K). Kruskal-Wallis test, $^{**}P < 0.001$ (J), $^{****}P < 0.0001$ (B and C), ns, not significant; two-tailed unpaired *t* test, $^{**}P = 0.0078$ (G), $^{****}P < 0.0001$ (K),.

To exclude the possibility that network contraction resulted from UtrCH-GFP expression, we labeled chromosomes and F-actin in fixed uninjected embryos. This confirmed the presence of a contractile F-actin network enclosing early prometaphase chromosomes (Fig. 2G). Notably, nuclear actin cables form a spatially discrete contractile network that is not continuous with cytoplasmic F-actin. Costaining for α-tubulin revealed that prometaphase microtubules are mostly peripheral to chromosomes during network contraction, in contrast to actin cables, which permeated the entire chromosomal region (Fig. 2G). This organization of prometaphase F-actin and microtubules in the early embryo counters that of centrosomal cell types, where the spindle is fully assembled by prometaphase and F-actin is largely excluded from the spindle zone (*34*) (fig. S2). These results suggest that, in the absence of centrosomes and efficient spindle assembly mechanisms, nuclear F-actin may drive the first stages of mitotic chromosome organization.

Nuclear actin cables organize mitotic chromosomes in the early embryo

We next evaluated the requirement of F-actin in chromosome organization and mitotic fidelity by treating embryos with cytochalasin D and imaging entire mitotic divisions. Cytochalasin D treatment eliminated chromosomal F-actin (fig. S3A) and impaired centripetal chromosome movement following NEBD (fig. S3, B to D). This treatment also delayed chromosome congression, increased mitotic duration (NEBD to anaphase), and increased the rate of chromosome missegregation (Fig. 3, A to D). Furthermore, centromeres in cytochalasin D–treated cells were often ejected toward the spindle poles. These centromeres did not return to the spindle equator, suggesting chromosome mono-orientation (fig. S3E and movie S5). This indicates that F-actin is required for mitotic fidelity and that spindle microtubules cannot functionally compensate for the lack of a chromosomal F-actin network in the early mouse embryo. To examine the function of F-actin independently of microtubules, we treated embryos with nocodazole and cytochalasin D, fixed the embryos, and imaged prometaphase-arrested cells. Although nocodazole treatment alone did not impair the reduction in chromosomal scattering volume following NEBD, treatment with both nocodazole and cytochalasin D markedly increased the scattering volume in prometaphase-arrested cells (Fig. 3, E to G), further indicating that actin filaments are necessary to drive the initial stages of chromosome organization.

The progressive shrinkage of the nuclear F-actin network suggests that it may be subject to contractile stress generated by nonmuscle myosin II (*35*). However, centripetal chromosome movement was unaffected in cells treated with blebbistatin or H1152, which inhibit actomyosin contractility (*36*) (fig. S3, B to D). We also imaged centripetal chromosome movement with <4-s temporal resolution to characterize contraction speed with increased precision. Similarly, myosin II inhibition did not impact the rate of network contraction (fig. S3, F to H). Blebbistatin treatment also failed to impair chromosome congression and chromosome segregation fidelity (Fig. 3, A to D). Thus, although myosin II is the principal driver of contractile force generation in organized actin assemblies, such as stress fibers and sarcomeres (*37*), the relative disorganization of nuclear actin may necessitate an alternative mechanism of force generation. Studies in other systems have shown that the contraction of cross-linked actin networks can also be achieved by filament depolymerization (*18*, *33*). We therefore manipulated F-actin polymerization rates and examined the effects on centripetal chromosome movement. We first treated embryos with jasplakinolide, which prevents F-actin depolymerization (*38*), and live-imaged cells entering mitosis. Jasplakinolide treatment markedly impaired centripetal chromosome movement, delayed chromosome congression, and increased the rate of chromosome missegregation (Fig. 3, A to D, and fig. S3, B to D).

These experiments indicate that cell-wide perturbations of F-actin polymerization are sufficient to impair network contraction and mitotic fidelity. To manipulate nuclear F-actin without perturbing cytoplasmic filaments, we expressed two nuclear localization signal (NLS)–containing actin mutants, yellow fluorescent protein (YFP)–NLS–β-actin $Gly^{13}Arg$ (NLS-actin-G13R) and YFP–NLS–β-actin $Ser^{14}Cys$ (NLS-actin-S14C), which promote ectopic filament depolymerization and stabilization, respectively (fig. S4, A to C) (*39*). In cells expressing NLS-actin-G13R, centripetal chromosome movement was significantly impaired following NEBD (fig. S4, D to F). This is consistent with the elimination of nuclear F-actin in these cells (fig. S4, A and B) and further suggests that centripetal chromosome movement is driven by the contraction of a nuclear F-actin network rather than protrusive forces generated outside of the nuclear region (*33*). Elimination of nuclear actin cables through NLS-actin-G13R expression resulted in delayed chromosome congression and chromosome missegregation (fig. S4, H to J). Stabilization of nuclear filaments through NLS-actin-S14C expression significantly impaired centripetal chromosome movement, consistent with a model whereby filament depolymerization is required for network contraction (fig. S4, D to F). NLS-actin-S14C expression also resulted in delayed chromosome congression and chromosome missegregation (fig. S4, H to J). Notably, the nuclear filaments in these cells were stably maintained following NEBD (fig. S4C).

To further dissect the role of filament depolymerization in network contraction, we treated embryos with low-dose latrunculin A and live-imaged chromosome dynamics following NEBD. This treatment enhances the rate of depolymerization-based network contraction by sequestering actin monomers and impairing filament elongation, thus shifting the net behavior of the system toward filament disassembly (*33*, *40*). Consistent with this model, latrunculin A treatment enhanced the speed and severity of centripetal chromosome movement following NEBD (Fig. 3, H to J). This suggests that filament disassembly drives network contraction following NEBD. We thus examined whether nuclear envelope disassembly alters the distribution of F-actin regulators, thereby promoting filament depolymerization and network contraction. Immunostaining for the actin nucleator formin-2 revealed a strong enrichment within the nucleus during interphase (Fig. 3, K and L, and fig. S5A). However, following NEBD, formin-2 was no longer enriched within the nuclear region (Fig. 3, K and L). Immunostaining for the diaphanous-related formin mDia2 revealed a similar enrichment within the interphase nucleus (fig. S5C). To further characterize the localization dynamics of nuclear formins, we live-imaged formin-2–GFP and mDia2-GFP during network contraction with <10-s temporal resolution. The nuclear intensity of both formins decreased sharply immediately before network contraction (fig. S5, B and D, and Movie S6).

These results suggest that formins promote nuclear F-actin assembly during interphase and that their regional dilution following NEBD attenuates the rate of filament elongation, thereby promoting filament disassembly and network contraction. We therefore utilized the pan-formin inhibitor SMIFH2 to evaluate the role of formins in network contraction. Consistent with the well-characterized role of nuclear formins (*20*, *41*), prolonged treatment with SMIFH2 reduced the density of nuclear actin cables during interphase (fig. S5E). Furthermore, SMIFH2 treatment immediately before mitosis resulted in the rapid coalescence of chromosomes upon NEBD, indicating a hypercontraction of the network (Fig. 3, H to J). This result suggests that the effects of SMIFH2, which has been reported to also inhibit members of the myosin superfamily (*42*), are unlikely to be attributed to off-target reactivity with myosin II.

Our results indicate that myosin II does not act as a nuclear filament cross-linker. We therefore evaluated the presence of alternative cross-linkers within the nucleus. The cross-linking protein anillin enhances the rate of disassembly-driven contraction in disordered F-actin networks (*40*). We identified a marked enrichment of anillin within the nucleus (fig. S5F), suggesting that anillin-dependent cross-linking may mediate network contraction. To evaluate the function of anillin, we

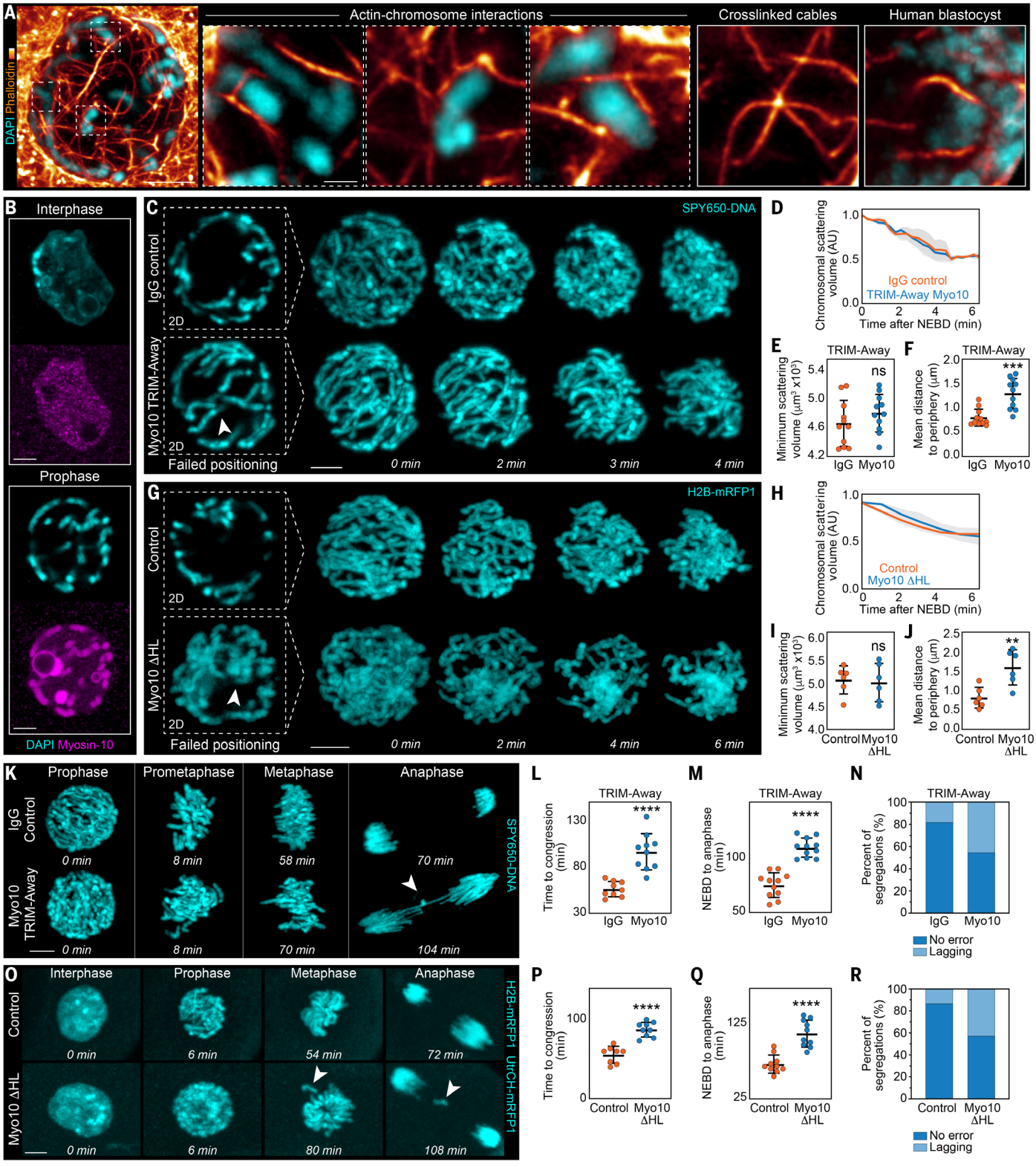

Fig. 4. F-actin–chromosome interactions are mediated by myosin-10. (**A**) Visualization of F-actin–chromosome interactions during prophase. Note the tethering of actin cables to prophase chromosomes. Images also highlight cross-linking of actin cables and similar structures in a human embryo (higher-magnification image of Fig. 1E). (**B**) Visualization of endogenous myosin-10 in interphase and prophase nuclei. (**C**) Live imaging of centripetal chromosome movement after depletion of endogenous myosin-10 through TRIM-Away. White arrows indicate chromosomes that fail to locate at the nuclear periphery. (**D**) Chromosomal scattering volume plotted over time. (**E**) Quantification of the minimum chromosomal scattering volume. IgG, immunoglobulin G. (**F**) Quantification of the mean distance of prophase chromosomes to the nuclear periphery. (**G**) Live imaging of centripetal chromosome movement in embryos expressing myosin-10 ΔHL. White arrows indicate chromosomes that fail to locate at the nuclear periphery. (**H**) Chromosomal scattering volume plotted over time. (**I**) Quantification of the minimum chromosomal scattering volume. (**J**) Quantification of the mean distance of prophase chromosomes to the nuclear periphery. (**K**) Live imaging of entire mitotic divisions in control and myosin-10–depleted embryos. (**L**) Quantification of chromosome congression

duration. (**M**) Quantification of mitotic duration (NEBD to anaphase). (**N**) Extent of chromosome segregation errors. (**O**) Live imaging of entire mitotic divisions in control and myosin-10 ΔHL–expressing embryos. White arrow highlights uncongressed and subsequent lagging chromosome. (**P**) Quantification of chromosome congression duration. (**Q**) Quantification of mitotic duration (NEBD to anaphase). (**R**) Extent of chromosome segregation errors. Scale bars, 5 μm [(A), (B), (C), (G), (K), and (O)]; 1 μm [(A), insets]. Sample sizes (embryos): 11 IgG control, 11 myosin-10 TRIM-Away [(D) to (F)]; 6 control, 6 myosin-10 ΔHL [(H) to (J)]; 9 IgG control, 10 myosin-10 TRIM-Away (L); 11 IgG control, 11 myosin-10 TRIM-Away [(M) and (N)]; 10 control, 10 myosin-10 ΔHL [(P) to (R)]. Two-tailed unpaired *t* test, $^{**}P < 0.01$ (J); $^{***}P < 0.001$ (F); $^{****}P < 0.0001$ [(L), (M), (N), (P), and (Q)]; ; ns, not significant [(E) and (I)].

implemented TRIM-Away, a method for degrading proteins in mouse oocytes and embryos (*43*) (fig. S5G). Consistent with its previously described role in myosin II–independent contraction (*40*), anillin degradation impaired centripetal chromosome movement following NEBD (fig. S5, H to J).

To further evaluate the contribution of filament depolymerization to network contraction, we analyzed the density and dynamics of actin cables following NEBD. During contraction, the density of actin cables remained constant (fig. S1, C and D). This conservation of cable density is incompatible with myosin II–driven contraction, where F-actin mass should remain constant in the shrinking network, leading to an increase in cable density (*18*). This finding suggests the presence of substantial filament turnover during network contraction. Cables in the interconnected nuclear actin network often displayed puncta at presumptive cable ends (Fig. 3M). We tracked these puncta to evaluate cable length over time. In the case of myosin II–driven contraction, cable shortening is achieved by the sliding of antiparallel filaments, where cables shorten symmetrically, and each cable end should exhibit similar speeds (*44*). However, we observed actin cables shortening with differing speeds at each end (Fig. 3M). This is consistent with the inherently asymmetric disassembly rates of barbed and pointed actin filament ends (*45*) and with a model whereby filament depolymerization drives network contraction. Thus, we propose that the contractile behavior of the nuclear F-actin network is governed by competing rates of filament elongation and depolymerization and that net filament disassembly can be attributed to a local dilution of formins following NEBD, which culminates in network contraction and centripetal chromosome movement.

F-actin positions mitotic chromosomes peripherally through myosin-10

We next investigated the mechanisms mediating actin-chromosome interactions during prophase and prometaphase (movie S7). In prophase mouse and human blastomeres, nuclear actin cables appeared to be physically coupled to chromosomes at the nuclear periphery (Fig. 4A). Given that peripheral chromosome organization is microtubule independent (Fig. 1J), we reasoned that the increase in actin polymerization during prophase may generate protrusive force, which transports chromosomes to the nuclear periphery. We next live-imaged cells expressing NLS-actin-G13R to evaluate the requirement of nuclear F-actin in prophase chromosome organization. Consistent with the elimination of nuclear actin cables, cells expressing NLS-actin-G13R failed to position prophase chromosomes at the nuclear periphery prior to NEBD (fig. S4, D and G). Furthermore, prophase chromosomes failed to individualize in the absence of nuclear F-actin and remained clustered in the center of the nucleus (fig. S4D).

We next evaluated the mechanism of actin-chromosome coupling. Previous experiments in *X. laevis* epithelia have shown that the unconventional motor myosin-10 localizes to interpolar microtubules and chromatin during mitosis (*46*). Immunostaining for endogenous myosin-10 in mouse embryos revealed a marked enrichment in the interphase nucleus and colocalization with prophase chromatin (Fig. 4B), suggesting that this motor may mediate actin-chromosome interactions. We implemented TRIM-Away to deplete endogenous myosin-10 (fig. S6, A and B). Myosin-10 depletion had no effect on the density of nuclear F-actin (fig. S6C). However, myosin-10–depleted cells failed to fully position chromosomes at the nuclear periphery prior to NEBD (Fig. 4, C and F). We also microinjected embryos with mRNA encoding a dominant-negative headless mutant myosin-10 ΔHL, which lacks the actin-binding motor domain (*47*). Cells expressing myosin-10 ΔHL similarly failed to fully position prophase chromosomes at the nuclear periphery (Fig. 4, G and J, and fig. S6D). These results suggest a model whereby actin polymerization and actin-chromosome coupling through myosin-10 organize prophase chromosomes at the nuclear periphery.

A ring-shaped chromosome arrangement facilitates amphitelic kinetochore attachment and promotes mitotic fidelity in centrosomal cell lines (*29*). We thus examined whether the peripheral organization of prophase chromosomes in the early mouse embryo functions analogously. We reasoned that the placement of chromosomes at the nuclear periphery may ensure that kinetochores are outward facing and not buried within the chromosome mass, thereby facilitating microtubule-kinetochore interactions following NEBD. Consistent with this rationale, myosin-10 depletion and myosin-10 ΔHL expression resulted in delayed chromosome congression, increased mitotic duration, and chromosome missegregation (Fig. 4, K to R). Furthermore, we frequently observed misaligned chromosomes during anaphase entry, suggesting the presence of monotelic or syntelic kinetochore attachments (Fig. 4, K and O). Together, these results indicate that nuclear F-actin and myosin-10 organize prophase chromosomes at the nuclear periphery to promote mitotic fidelity.

The minimum chromosomal scattering volume remained unaffected following myosin-10 perturbation (Fig. 4, D, E, H, and I), suggesting that myosin-10 may be dispensable for actin-chromosome coupling during network contraction. To evaluate whether nonspecific actin-chromosome interactions are sufficient to couple chromosomes to the contracting network, we quantified the network pore size in phalloidin-labeled embryos, which yielded an average pore area of $0.665 \pm 0.186\ \mu m^2$ during prophase and $0.663 \pm 0.151\ \mu m^2$ during prometaphase (fig. S1D). This pore size is significantly smaller than mitotic chromosomes at the two-cell stage, which have a length of 7.35 ± 2.49 μm and a cross-sectional area of $8.07 \pm 2.43\ \mu m^2$. This suggests that chromosomal motors are likely dispensable for actin-chromosome coupling during network contraction, as the small pore size of the network renders chromosome escape unlikely. We thus propose that nonspecific steric trapping is sufficient to couple chromosomes to the contracting network, similar to a previously observed mechanism in starfish oocytes (*33*).

Perispindle F-actin controls spindle size

We finally investigated the role of F-actin following spindle assembly. In somatic cells, spindle size is typically regulated by centrosomes and astral microtubules (*2*, *48*–*50*). However, acentrosomal spindles in the two-cell mouse embryo do not display astral microtubules (*30*, *31*), raising the question of how spindle size is regulated during early development (movie S8). We imaged phalloidin-labeled embryos and identified a distinct F-actin network that assembles in the cell center and encloses the metaphase spindle (Fig. 5A). In contrast to the cable-like morphology of nuclear actin, perispindle F-actin displays a dense patch-like morphology resembling branched actin. We thus evaluated the role of the Arp2/3 complex in perispindle F-actin nucleation. Immunostaining of Arp3 revealed a prominent enrichment at the metaphase spindle periphery (Fig. 5B). Moreover, embryos expressing exogenous Arp3-GFP displayed a similar localization pattern (Fig. 5C). Treatment with the Arp2/3 complex inhibitor CK-666 (*51*) reduced the

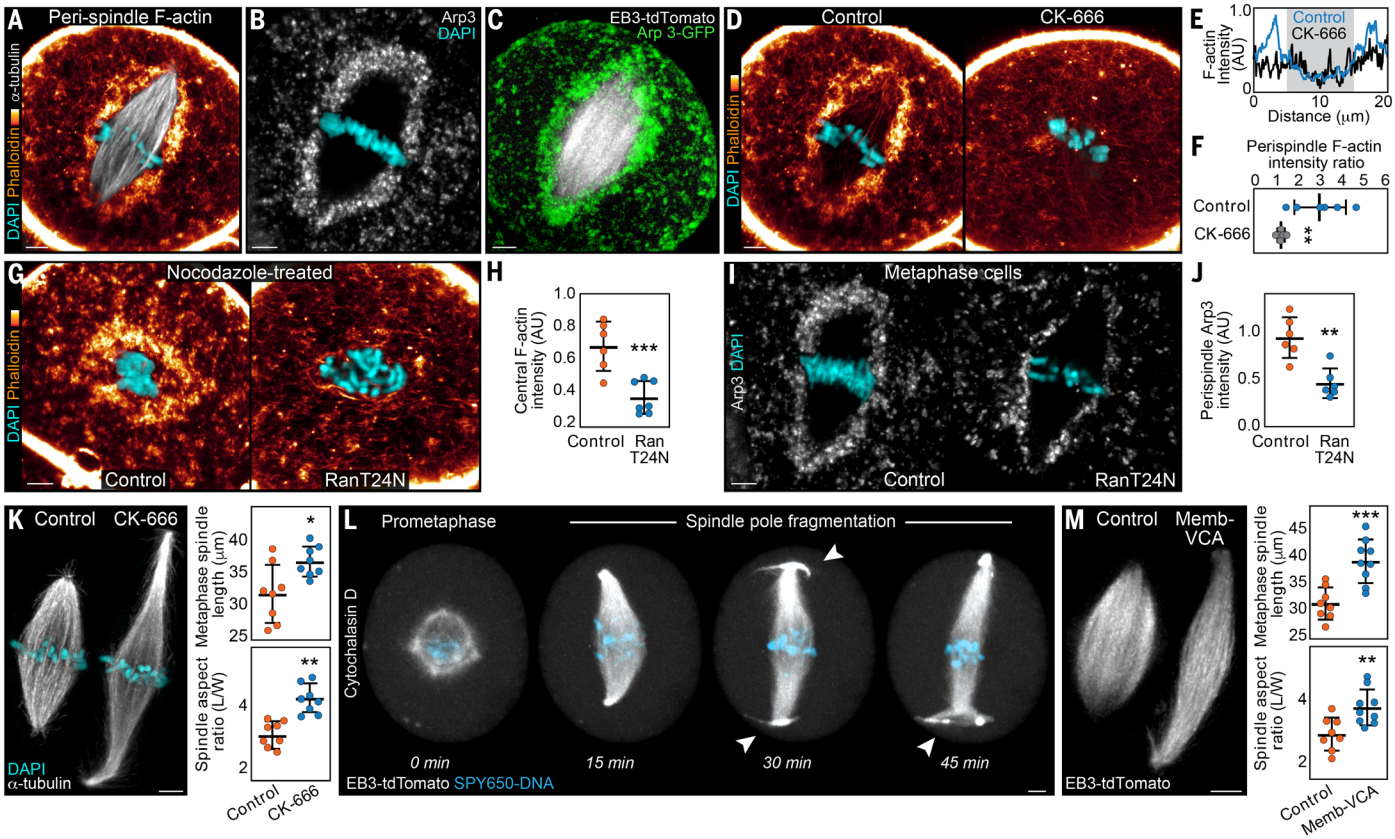

Fig. 5. Perispindle F-actin controls spindle size and morphology. (**A**) Visualization of perispindle F-actin in a control metaphase cell. (**B**) Visualization of endogenous Arp3 in a metaphase two-cell blastomere. Note the enrichment of Arp3 at the spindle periphery. (**C**) A two-cell mouse blastomere expressing Arp3-GFP and EB3-tdTomato. Note the accumulation of Arp3-GFP around the metaphase spindle. (**D**) Visualization of metaphase F-actin in control and CK-666–treated cells. (**E**) Mean Phalloidin intensity profiles of control and CK-666–treated embryos. (**F**) Perispindle F-actin intensity ratios. (**G**) Visualization of F-actin and chromosomes in nocodazole-treated cells. Note the F-actin enrichment proximal to mitotic chromatin in the control cell. F-actin distribution appears homogenous in the Ran^{T24N}-expressing cell. (**H**) Quantification of central F-actin density. (**I**) Visualization of endogenous Arp3 in metaphase control and Ran^{T24N}-expressing cells. (**J**) Quantification of perispindle Arp3 enrichment in metaphase control and Ran^{T24N}-expressing cells. (**K**) Metaphase spindles in control and CK-666–treated embryos. Quantification of spindle size and morphology. (**L**) Live imaging of spindle assembly in an embryo treated with cytochalasin D. White arrows indicate spindle pole fragmentation. (**M**) Metaphase spindles in live embryos expressing memb-VCA. Quantification of spindle size and morphology. Scale bars, 5 μm [(A), (B), (C), (D), (G), (I), (K), (L), and (M)]. Sample sizes (embryos): 6 control, 6 CK-666 [(E) and (F)]; 6 control (sham injection), 7 Ran^{T24N} (H); 6 control (sham injection), 7 Ran^{T24N} (J); 8 control, 8 CK-666 (K); 8 control (memb-GFP), 9 memb-VCA (M). Statistical tests: two-tailed unpaired *t* test, $*P = 0.0143$ (K top); $**P < 0.01$ [(F); (J); (K), bottom; and (M), bottom); $***P < 0.001$ [(H) and (M), top].

density of perispindle F-actin (Fig. 5, D to F), further indicating that the network is composed of branched filaments. Unlike the mouse embryo, we did not detect a significant enrichment of F-actin at the spindle periphery in human blastocysts (fig. S7A).

In contrast to metaphase F-actin organization, interphase F-actin is homogenously distributed throughout the cytoplasm (fig. S1A). This indicates that a mitosis-specific mechanism drives the symmetry breaking of F-actin organization, leading to F-actin nucleation near the cell center. Previous studies in mouse oocytes have shown that a chromatin-derived gradient of guanosine triphosphaste (GTP)–bound Ran (RanGTP) induces local Arp2/3 complex activation (*52*). We thus visualized F-actin in nocodazole-treated cells to examine the relationship between F-actin organization and mitotic chromatin. Phalloidin-labeled cells displayed a marked accumulation of F-actin proximal to mitotic chromatin (Fig. 5G), suggesting that chromatin-derived signals may promote filament nucleation near the cell center. We next evaluated the role of RanGTP by injecting embryos with mRNA encoding a dominant-negative version of the Ran GTPase (Ran^{T24N}; T, Thr; N, Asn). In nocodazole-treated cells, Ran^{T24N} expression significantly reduced the intensity of F-actin proximal to mitotic chromatin (Fig. 5, G and H). Ran^{T24N} expression also decreased the density of endogenous Arp3 at the metaphase spindle periphery (Fig. 5, I and J). Therefore, chromatin-derived RanGTP promotes Arp2/3-mediated F-actin nucleation at the metaphase spindle periphery.

The finding of branched F-actin adjacent to microtubules is reminiscent of work describing centrosomal actin, which attenuates microtubule elongation in an Arp2/3-dependent manner (*53*). In vitro reconstitution experiments have also shown that branched F-actin blocks the growth of microtubules and triggers their disassembly (*54*). We thus examined whether perispindle F-actin functions analogously, by regulating mitotic spindle size in the absence of centrosomes. We first determined how manipulations of Arp2/3 complex activity impact spindle size and morphology. CK-666 treatment resulted in the marked overgrowth of metaphase spindles (Fig. 5K). Metaphase spindles in CK-666–treated cells deviated from the characteristic barrel shape of cleavage-stage spindles (*55*) and assumed a thinner morphology with a higher aspect ratio (Fig. 5K). We also observed unrestricted spindle lengthening and spindle pole fragmentation following treatment with cytochalasin D (Fig. 5L and fig. S7B), further indicating that the maintenance of spindle length and morphology is F-actin-dependent. To further perturb the function of the Arp2/3 complex, we overexpressed a membrane-anchored version of the Arp2/3 complex–activating

verprolin- and cofilin-homology acidic (memb-VCA) construct (56). Memb-VCA overexpression similarly diminished the density of perispindle F-actin (fig. S7C), likely through the membrane sequestration of Arp2/3 complex members. As a result, metaphase spindles displayed unrestricted elongation, with spindle poles often reaching the cortex (Fig. 5M).

Discussion

The lack of efficient spindle assembly mechanisms poses a major challenge to mitotic cell divisions during early mammalian development. Our study reveals two distinct actin assemblies that ensure mitotic fidelity throughout the duration of mitosis (fig. S8). Unlike centrosomal cell types, the mitotic spindle in the early embryo does not exhibit bipolar organization or a well-defined spindle equator until late prometaphase. Thus, in lieu of a fully assembled spindle, a nuclear F-actin network contracts and ensures that chromosomes are partially congressed prior to spindle assembly. Furthermore, we propose that centripetal chromosome movement likely promotes microtubule nucleation by increasing the spatial density of chromosomally localized RCC1 protein, which activates Ran (57).

F-actin–dependent chromosome positioning notably solves a major challenge associated with the unusually large mitotic chromosomes and weak microtubule organizing centers of the early embryo. In centrosomal cell types, microtubules emanating from centrosomes exert polar ejection forces (PEFs) on chromosome arms, mediating their congression toward the metaphase plate (58). Because the effectiveness of PEFs increases with higher microtubule density and smaller chromosome size (59), the early embryo represents a system in which PEFs might be rendered ineffective.

The mechanisms of actin-chromosome coupling in the early mouse embryo differ from those reported in oocytes. In this work, we described myosin-10 as a chromosomal motor that mediates actin-based chromosome positioning. By contrast, actin-chromosome interactions in starfish oocytes are largely mediated by chromosomal F-actin patches (18), and work in mammalian oocytes has suggested that actin cables interact with kinetochores (20). A meiotic chromosomal F-actin motor analogous to myosin-10 therefore remains unidentified. Additionally, chromosomal F-actin in starfish oocytes is only detected following NEBD (*18*, *20*). Instead, our data revealed that interphase nuclear actin cables are maintained through mitotic entry, where they serve essential functions following NEBD.

Our finding of branched F-actin at the spindle periphery suggests that, in the absence of centrosomes and astral microtubules, perispindle F-actin functions as a provisional mechanism to modulate spindle size. Furthermore, this suggests that spindle size in large acentriolar cells may not be determined by an intrinsic upper limit (*31*) but by a physical process whereby branched F-actin functions as a brake-like mechanism during the elongation phase of spindle assembly (*54*). Our study highlights the versatility of the actin cytoskeleton during preimplantation development, where it compensates for the lack of efficient spindle assembly mechanisms, underscoring the remarkable robustness of the developmental program.

Materials and methods

Ethical approval

This research complies with all relevant ethical regulations, including review and approval of all mouse work from the Institutional Animal Care and Use Committee (IACUC) of the University of Pennsylvania (Protocol #806983) and review and approval of donated human embryo work by the New England Institutional Review Board (WO 1-6450-1).

Mouse embryo work

Superovulated wild-type female mice at 8 weeks of age were used following animal ethics guidelines of the University of Pennsylvania IACUC. Approximately five female mice were used per experimental replicate. Superovulation was performed using 5 international units (IU) of pregnant mare serum (PMS, National Hormone and Peptide Program) gonadotropin given intraperitoneally and 5 IU of recombinant chorionic gonadotrophin (CG, National Hormone and Peptide Program) given 48 hours after and immediately before mating. The embryos used in our experiments were derived from Hsd:NSA(CF-1), but we also validated the presence of nuclear actin in FVB/NTac, C57BL/6JInv, and IcrTac:ICR backgrounds. Animals were purchased from approved vendors (i.e., Charles Rivers Laboratories, Envigo and Jackson Laboratory). All mice were maintained within a BSL2 animal facility at the University of Pennsylvania in pathogen-free conditions with access to water and food ad libitum, a 12-hour dark/12-hour light cycle between 07:00 and 19:00 in a temperature (68° to 76°F) and humidity (30 to 70%) controlled room.

Embryos were flushed from oviducts with M2 medium (Merck) and cultured in KSOM + AA (Merck) covered by mineral oil (Sigma) at 37°C and 5% CO_2. Live embryos were microinjected with 0.1 to 0.3 pL RNA in injection buffer (5 mM Tris, 5 mM NaCl, 0.1 mM EDTA) using a FemtoJet (Eppendorf). For live imaging, embryos were cultured in 8-well μ-Slides (Ibidi) at 37°C and 5% CO_2 in an incubator adapted for the microscope system (Carl Zeiss LSM780, LSM880 and Leica SP8). Expression constructs were cloned into pCS2+ or pGEMHE backbones for mRNA production. The mMESSAGE mMACHINE® SP6 and T7 kits (Ambion) were used to synthesize RNA using linearized plasmids as templates following manufacturer's instructions. RNA was purified using RNAeasy kit (Qiagen) following manufacturer's instructions. Embryos were microinjected with mRNA encoding: H2B-mRFP1 at 5 ng μl^{-1}; GFP-UtrCH at 70 ng μl^{-1}; Formin 2–GFP at 50 ng μl^{-1}; EB3-tdTomato at 50 ng μl^{-1}; mClover3-MAP4-MTBD at 2 ng μl^{-1}; mEmerald-Myosin-10 DHL at 60 ng μl^{-1}; Ran-T24N-mRFP1 at 80 ng μl^{-1}; YFP NLS-actin-S14C at 120 ng μl^{-1}; YFP NLS-actin-G13R at 200 ng μl^{-1}; mClover3-Maj sat-TALE at 30 ng μl^{-1}.

Generation of nuclei acid constructs

The generation of constructs for myosin-10 DHL expression was previously described (*60*). The full length pCS2+ myosin-10 construct was cloned from mouse embryonic fibroblast complementary DNA (cDNA). Full-length mouse myosin-10 was cloned into a pCS2+ backbone, downstream of the SP6 promoter, by Gibson assembly utilizing the primers 5′-ATTCAAGGCCTCTCGAGCCTATGGACAGCTTCTTTCCCGAG-3′ and 5′-TAATACGACTCACTATAGTTTCACCTGGAGCTGCCCTG-3′. Arp3-GFP (from M. Welch, UC Berkeley, USA, Addgene #8462) and GFP-mDia2 (from A. Alberts, UC San Francisco, USA, Addgene #25407) were cloned into a pCS2+ backbone downstream of the SP6 promoter. To generate membrane-GFP-VCA, the VCA domain of EzrinTD-mCherry-VCA (gift from Marie-Hélène Verlhac and Marie-Emilie Terret) was amplified by PCR and cloned downstream of membrane-GFP (from A. Hamdoun, UC San Diego, USA, Addgene #198056) via Gibson assembly. To express YFP NLS-actin-S14C (*39*) (from D. Knipe, Harvard Medical School, USA, Addgene #60615) and YFP NLS-actin-G13R (from D. Knipe, Harvard Medical School, USA, Addgene #60614) in embryos, the open reading frames (ORFs) of each construct were cloned into the pCS2+ backbone, downstream of the SP6 promoter. Briefly, pCS2+ vector was linearized by XbaI restriction digest. The ORFs from YFP NLS-actin-S14C (Addgene #60614) and YFP NLS-actin-G13R (Addgene #60615) were transferred into pCS2+ by Gibson assembly using identical primers: 5′-ATTCAAG GCCTCTCGAGCCTATGGTGAGCAAGGGCGAG-3′ and 5′-TAATACGACTC ACTATAGTTCTAGAAGCATTTGCGGTGG-3′.

Transient nucleic acid transfection

Transient small interfering RNA (siRNA) transfection of C2C12 mouse myoblasts was performed using 12 nM non-targeting siRNA (Dharmacon, ON-TARGETplus Non-targeting Control siRNAs, D-001810-01) and 12 nM myosin-10 siRNA (Dharmacon, ON-TARGETplus Mouse Myo10 siRNA,

L-062004-01) complexed with Lipofectamine RNAiMAX (ThermoFisher, 13778100) in Opti-MEM (Gibco, 31985070). Plasmid DNA (pCS2+ myosin-10 tagless) was complexed with FuGENE 6 (Promega, E269A) at a 1:3 ratio in Opti-MEM. After a 15-min incubation, the transfection solution was added to the culture medium.

Endogenous protein degradation

For TRIM-Away (*43*) concentrated antibodies (Mouse IgG; Sigma, #12-371, myosin-10; Novus Biologicals, 22430002; and Anillin ;Thermo Scientific, PA5114851) were injected into 1-cell embryos at 0.3 μg/μl, along with 400 ng/μl mCherry-TRIM21 mRNA.

Dyes and drug treatments

For labeling of genomic DNA, live embryos were incubated with SPY650-DNA (Cytoskeleton, SC501) for 1 hour at 1:1000. Following incubation, the medium was replaced and embryos were imaged immediately. For drug treatments in Fig. 3, A to D, the following concentrations were used: Cytochalasin D (Tocris, 1233) at 2 μg/ml, (*S*)-(-)-Blebbistatin (Tocris, 1852) at 25 μM, H1152 (Tocris, 2414) at 25 μM, Jasplakinolide (Tocris, 2792) at 5 μM. For these experiments, drug was applied during late interphase, and embryos were imaged after 1 hour incubation. For the experiments in Fig. 3H, SMIFH2 (Tocris, 4401) at 100 μM and Latrunculin A (Tocris, 3973) at 500 nM were applied <20 min before imaging in order to avoid complete network depolymerization. For Figs. 1G and 3, E to G, Nocodazole (Tocris, 1228) was added to the media at 50 ng/ml. For all vehicle control experiments, dimethyl sulfoxide (DMSO) was added the media at concentrations equivalent to treatment groups.

Immunoblotting

C2C12 cells were lysed in radioimmunoprecipitation assay buffer plus protease inhibitor cocktail (Sigma, P8340), phosphatase inhibitor cocktail #2 (Sigma, P5726) and #3 (Sigma, P0044), used at 1:100 each. Supernatants were collected after centrifugation at 14,000 rotations per minute for 15 min at 4°C, adjusted to 1x laemmli sample buffer and then subjected to SDS-PAGE. Antibodies for immunoblotting were purchased from the following vendors: anti-GAPDH (2118) from Cell Signaling Technology, Myosin-10 from Novus.

Immunofluorescence

For labeling of F-actin and microtubules in fixed embryos, embryos were simultaneously extracted and fixed with 0.2% glutaraldehyde in a fixation buffer consisting of 0.5% Triton X-100, and PEM (80 mM PIPES, 5 mM EGTA, 2 mM MgCl2, pH 6.8) (*61*) for 10 min at 37°C. Embryos were subsequently quenched in 1 mg/ml Sodium Borohydride for 7 min to reduce autofluorescence, then briefly washed three times in PBS w/ 0.1% Triton X-100 (PBT). For immunolabeling of endogenous formin-2 and myosin-10, embryos were fixed in 4% Paraformaldehyde (in PBS) for 20 min at 37°C and washed 3 times in 0.1% PBT. Embryos were blocked in 3% BSA w/ 0.1% PBT for 30 min at room temperature, then incubated in primary antibody solution overnight at 4 °C at the following concentrations: α-tubulin (Sigma, T6199) at 1:200; formin-2 (Invitrogen, PA5- 65632 and Atlas antibodies, HPA050649) at 1:300; Anillin (Thermo Scientific, PA5114851) at 1:200; Arp3 (Abcam, ab49671) at 1:60; mDia2 (ECM biosciences, DP3491) at 1:100; myosin-10 (Novus Biologicals) at 1:400. Following primary antibody incubation, embryos were washed 5 times in 0.1% PBT for a total of 2 hours or longer. Samples were incubated with pre-centrifuged Alexa Fluor 647-conjugated secondary antibodies (A32728, A32733) at 1:400 for 30 min. Embryos were then washed 3 times in 0.1% PBT for a total of 1 hour or longer. For labeling of the actin cytoskeleton, embryos were incubated in Phalloidin Alexa Fluor 488 at 1:50 for 50 min, then briefly washed in 0.1% PBT before imaging. To label chromosomes, fixed embryos were incubated with 4′,6-diamidino-2-phenylindole (DAPI; Sigma, 10236276001) at 1:1000, and briefly washed in 0.1% PBT. Embryos which were imaged with a water immersion objective were mounted in 0.1% PBT. For higher-resolution imaging, embryos and cell lines were mounted in 95% glycerol and imaged with an oil-immersion objective.

Imaging

Fixed specimens were imaged using a laser scanning confocal microscope (Leica SP8) with a 40× 1.1 NA Apochromat water-immersion objective, or a 63× 1.4 NA Apochromat oil-immersion objective. Samples were excited with standard laser lines (405, 488, 552, and 638 nm), and images were acquired with Nyquist-optimized sampling. Live embryos were imaged using a 40× 1.1 NA Apochromat water-immersion objective. For long-term imaging of the entire cell division process, images were acquired using 512 × 512 sampling, 16× to 32× line averaging, and a pinhole size of 1.5 Airy units or higher. For short-term imaging experiments, images were acquired using Nyquist-optimized sampling, and a pinhole size of 1.5 AU or lower. Some images were cropped in order to remove extra-cytoplasmic or extra-nuclear signal when appropriate.

Actin cable and microtubule density measurements

Three-dimensional (3D) visualizations and analyses of embryos were performed using Imaris 8.2 or Imaris 9.7 software (Bitplane). For analysis of nuclear actin cable density, a mask of the nuclear region was acquired by using the semiautomatic (interphase nuclei) or manual segmentation (prophase nuclei) modes. The length of nuclear actin cables was manually quantified using the point tool in Imaris. The total length of all cables was then divided by the volume of the nuclear compartment. The width of the cables was not factored into the analyses, as the degree of filament bundling cannot be accurately determined by confocal microscopy (*34*).

For Fig. 1B, 1-μm z-stacks were processed in two dimensions. To analyze network density, then cytoplasmic signal was removed by tracing a line around the network and applying the "clear outside" function in ImageJ. Ridge detection was performed on the Phalloidin signal to extract cable lengths, and the network density was calculated by dividing the summed cable lengths by the network area.

To analyze the void dimensions of prophase and prometaphase F-actin networks, we utilized a previously described workflow, which models network voids as circular pores (*34*). We processed z-stacks of thickness ~1 μm in two dimensions, which approximates the thickness of mitotic chromosomes (~1.2 μm). In brief, we performed ridge detection to segment actin cables, then inverted the binary segmentation image, essentially segmenting the inter-cable regions or "pores." The distance map was then computed, and the value of the maximum eroded point of each pore segmentation was recorded to extract the corresponding pore radius. The circular pore area was then calculated.

Mitotic duration quantification

The length of NEBD to anaphase was defined as the duration between the first frame of prometaphase and the first frame of anaphase. The time to chromosome congression was defined as the duration between the first frame of prometaphase and the frame where chromosomes achieved stable alignment at the metaphase plate. Chromosomes were only considered to be congressed if they remained at the metaphase plate and were not ejected toward the spindle pole. In the case of cells containing uncongressed chromosomes during anaphase induction, the duration between NEBD to anaphase was recorded.

Chromosome distance to nuclear periphery

To evaluate the organization of prophase chromosomes in live embryos (e.g., Fig. 1, G and J), the final prophase timepoint (immediately before NEBD) was analyzed. For all groups, a three-slice maximum intensity projection corresponding to the center of the nucleus was processed in two dimensions. The chromosome signal was segmented and the binary segmentation image was then multiplied by a distance map of

the nuclear periphery (fig. S1J). The resulting image was then exported, and the mean of all nonzero values was calculated.

Convex hull area and volume quantification

We modeled chromosomal scattering volume by computing the convex hull (the smallest convex set which contains a given object) of segmented chromosomes (fig. S1I) (*62*). To quantify chromosomal scattering volume in four dimensions, the convex hull was computed using signal from SPY650-DNA or H2B-mRFP1 signal. In ImageJ, a 3×3–pixel median filter and bleach correction were applied, a 4D time series was split into individual 3D stacks, and each 3D stack was thresholded using the 3D Objects Counter plugin. In MATLAB, the 3D convex hull, and its volume, were computed for each segmentation image and plotted over time (https://github.com/PlachtaLab/Hernandez-et-al-2025) (*63*). The "minimum scattering volume" corresponds to the lowest value over the plotted time period. For fixed imaging experiments, the same procedure was performed on images of prometaphase-arrested cells. For Figs. 2, D and E, 2D spatial analysis was performed on maximum intensity projections generated from ~4-μm stacks. Briefly, high-intensity puncta in the UtrCH-GFP channel were manually tracked in ImageJ using the TrackMate plugin. Spatial coordinates for all tracks were then exported into MATLAB. For each time slice, the 2D convex hull of the tracked coordinates was calculated, and its area was plotted over time.

Perispindle intensity ratio analysis

To evaluate perispindle actin intensity, the line tool in ImageJ was used to draw a 20-μm line along the metaphase plate. The x axis (distance) of the intensity plots were divided into quadrants, with the outer quadrants being defined as spindle peripheral zones. The area under the curve (AUC) was computed for each quadrant. The summed areas of quadrants 1 and 4 (perispindle quadrants) were then divided by the summed areas of quadrants 2 and 3 (inner quadrants).

Experimental design

No statistical methods were used to predetermine sample size. Following isolation, embryos were randomly allocated to experimental groups. Investigators were blinded to experimental groups during data analysis. Only embryos exhibiting normal developmental morphology were used for experiments.

Statistics and reproducibility

Statistical analyses were performed in Excel and GraphPad Prism. Data were analyzed for normality using a D'Agostino-Pearson omnibus normality test. Variables displaying a normal distribution were analyzed using an unpaired, two-tailed Student's t test for two groups, and analysis of variance with Dunnett's multiple comparisons test for more than two groups. Variables that did not follow a normal distribution were analyzed using an unpaired, two-tailed Mann-Whitney U test for two groups, and Kruskal-Wallis test with Dunn's multiple comparisons test for more than two groups. Reproducibility was confirmed by at least three independent experiments.

REFERENCES AND NOTES

1. R. Li, J. Zhu, Effects of aneuploidy on cell behaviour and function. *Nat. Rev. Mol. Cell Biol.* **23**, 250–265 (2022). doi: 10.1038/s41580-021-00436-9; pmid: 34987171
2. S. Dumont, T. J. Mitchison, Force and length in the mitotic spindle. *Curr. Biol.* **19**, R749–R761 (2009). doi: 10.1016/j.cub.2009.07.028; pmid: 19906577
3. A. A. Hyman, E. Karsenti, Morphogenetic properties of microtubules and mitotic spindle assembly. *Cell* **84**, 401–410 (1996). doi: 10.1016/S0092-8674(00)81285-4; pmid: 8608594
4. R. Heald, A. Khodjakov, Thirty years of search and capture: The complex simplicity of mitotic spindle assembly. *J. Cell Biol.* **211**, 1103–1111 (2015). doi: 10.1083/jcb.201510015; pmid: 26668328
5. G. Manandhar, H. Schatten, P. Sutovsky, Centrosome reduction during gametogenesis and its significance. *Biol. Reprod.* **72**, 2–13 (2005). doi: 10.1095/biolreprod.104.031245; pmid: 15385423
6. G. Manandhar, C. Simerly, J. L. Salisbury, G. Schatten, Centriole and centrin degeneration during mouse spermiogenesis. *Cell Motil. Cytoskeleton* **43**, 137–144 (1999). doi: 10.1002/(SICI)1097-0169(1999)43:2<137::AID-CM5>3.0.CO;2-7; pmid: 10379838
7. H. Schatten, The mammalian centrosome and its functional significance. *Histochem. Cell Biol.* **129**, 667–686 (2008). doi: 10.1007/s00418-008-0427-6; pmid: 18437411
8. D. Clift, M. Schuh, A three-step MTOC fragmentation mechanism facilitates bipolar spindle assembly in mouse oocytes. *Nat. Commun.* **6**, 7217 (2015). doi: 10.1038/ncomms8217; pmid: 26147444
9. C. Gueth-Hallonet *et al.*, gamma-Tubulin is present in acentriolar MTOCs during early mouse development. *J. Cell Sci.* **105**, 157–166 (1993). doi: 10.1242/jcs.105.1.157; pmid: 8360270
10. C. E. Currie *et al.*, The first mitotic division of human embryos is highly error prone. *Nat. Commun.* **13**, 6755 (2022). doi: 10.1038/s41467-022-34294-6; pmid: 36347869
11. K. Scheffler *et al.*, Two mechanisms drive pronuclear migration in mouse zygotes. *Nat. Commun.* **12**, 841 (2021). doi: 10.1038/s41467-021-21020-x; pmid: 33547291
12. A. Chaigne *et al.*, A soft cortex is essential for asymmetric spindle positioning in mouse oocytes. *Nat. Cell Biol.* **15**, 958–966 (2013). doi: 10.1038/ncb2799; pmid: 23851486
13. K. Yi *et al.*, Dynamic maintenance of asymmetric meiotic spindle position through Arp2/3-complex-driven cytoplasmic streaming in mouse oocytes. *Nat. Cell Biol.* **13**, 1252–1258 (2011). doi: 10.1038/ncb2320; pmid: 21874009
14. A. Chaigne *et al.*, A narrow window of cortical tension guides asymmetric spindle positioning in the mouse oocyte. *Nat. Commun.* **6**, 6027 (2015). doi: 10.1038/ncomms7027; pmid: 25597399
15. K. Yi *et al.*, Sequential actin-based pushing forces drive meiosis I chromosome migration and symmetry breaking in oocytes. *J. Cell Biol.* **200**, 567–576 (2013). doi: 10.1083/jcb.201211068; pmid: 23439682
16. H. Wang *et al.*, Dual control of formin-nucleated actin assembly by the chromatin and ER in mouse oocytes. *Curr. Biol.* **32**, 4013–4024.e6 (2022). doi: 10.1016/j.cub.2022.07.058; pmid: 35981539
17. J. Azoury *et al.*, Spindle positioning in mouse oocytes relies on a dynamic meshwork of actin filaments. *Curr. Biol.* **18**, 1514–1519 (2008). doi: 10.1016/j.cub.2008.08.044; pmid: 18848445
18. P. Lénárt *et al.*, A contractile nuclear actin network drives chromosome congression in oocytes. *Nature* **436**, 812–818 (2005). doi: 10.1038/nature03810; pmid: 16015286
19. M. Burdyniuk, A. Callegari, M. Mori, F. Nédélec, P. Lénárt, F-Actin nucleated on chromosomes coordinates their capture by microtubules in oocyte meiosis. *J. Cell Biol.* **217**, 2661–2674 (2018). doi: 10.1083/jcb.201802080; pmid: 29903878
20. K. Harasimov *et al.*, Actin-driven chromosome clustering facilitates fast and complete chromosome capture in mammalian oocytes. *Nat. Cell Biol.* **25**, 439–452 (2023). doi: 10.1038/s41556-022-01082-9; pmid: 36732633
21. B. Mogessie, M. Schuh, Actin protects mammalian eggs against chromosome segregation errors. *Science* **357**, eaal1647 (2017). doi: 10.1126/science.aal1647; pmid: 28839045
22. J. Roeles, G. Tsiavaliaris, Actin-microtubule interplay coordinates spindle assembly in human oocytes. *Nat. Commun.* **10**, 4651 (2019). doi: 10.1038/s41467-019-12674-9; pmid: 31604948
23. A. M. Kita *et al.*, Spindle-F-actin interactions in mitotic spindles in an intact vertebrate epithelium. *Mol. Biol. Cell* **30**, 1645–1654 (2019). doi: 10.1091/mbc.E19-02-0126; pmid: 31091161
24. H. Oda *et al.*, Actin filaments accumulated in the nucleus remain in the vicinity of condensing chromosomes in the zebrafish early embryo. *Biol. Open* **12**, bio059783 (2023). doi: 10.1242/bio.059783; pmid: 37071022
25. J. C. Sandquist, A. M. Kita, W. M. Bement, And the dead shall rise: Actin and myosin return to the spindle. *Dev. Cell* **21**, 410–419 (2011). doi: 10.1016/j.devcel.2011.07.018; pmid: 21920311
26. L. M. G. Paim, G. FitzHarris, Tetraploidy causes chromosomal instability in acentriolar mouse embryos. *Nat. Commun.* **10**, 4834 (2019). doi: 10.1038/s41467-019-12772-8; pmid: 31645568
27. A. D. Macaulay, A. Allais, G. FitzHarris, Chromosome dynamics and spindle microtubule establishment in mouse embryos. *FASEB J.* **34**, 8057–8067 (2020). doi: 10.1096/fj.201902947R; pmid: 32329130
28. T. Okuno *et al.*, Zygotic Nuclear F-Actin Safeguards Embryonic Development. *Cell Rep.* **31**, 107824 (2020). doi: 10.1016/j.celrep.2020.107824; pmid: 32610125
29. V. Magidson *et al.*, The spatial arrangement of chromosomes during prometaphase facilitates spindle assembly. *Cell* **146**, 555–567 (2011). doi: 10.1016/j.cell.2011.07.012; pmid: 21854981
30. O. Pomp *et al.*, A monoastral mitotic spindle determines lineage fate and position in the mouse embryo. *Nat. Cell Biol.* **24**, 155–167 (2022). doi: 10.1038/s41556-021-00826-3; pmid: 35102267
31. A. Courtois, M. Schuh, J. Ellenberg, T. Hiiragi, The transition from meiotic to mitotic spindle assembly is gradual during early mammalian development. *J. Cell Biol.* **198**, 357–370 (2012). doi: 10.1083/jcb.201202135; pmid: 22851319

32. B. M. Burkel, G. von Dassow, W. M. Bement, Versatile fluorescent probes for actin filaments based on the actin-binding domain of utrophin. *Cell Motil. Cytoskeleton* **64**, 822–832 (2007). doi: 10.1002/cm.20226; pmid: 17685442
33. P. Bun, S. Dmitrieff, J. M. Belmonte, F. J. Nédélec, P. Lénárt, A disassembly-driven mechanism explains F-actin-mediated chromosome transport in starfish oocytes. *eLife* **7**, e31469 (2018). doi: 10.7554/eLife.31469; pmid: 29350616
34. A. S. Moore *et al.*, Actin cables and comet tails organize mitochondrial networks in mitosis. *Nature* **591**, 659–664 (2021). doi: 10.1038/s41586-021-03309-5; pmid: 33658713
35. G. Lee *et al.*, Myosin-driven actin-microtubule networks exhibit self-organized contractile dynamics. *Sci. Adv.* **7**, eabe4334 (2021). doi: 10.1126/sciadv.abe4334; pmid: 33547082
36. J. Zenker *et al.*, Expanding Actin Rings Zipper the Mouse Embryo for Blastocyst Formation. *Cell* **173**, 776–791.e17 (2018). doi: 10.1016/j.cell.2018.02.035; pmid: 29576449
37. A. F. Huxley, R. Niedergerke, Structural changes in muscle during contraction; interference microscopy of living muscle fibres. *Nature* **173**, 971–973 (1954). doi: 10.1038/173971a0; pmid: 13165697
38. A. Holzinger, Jasplakinolide. An actin-specific reagent that promotes actin polymerization. *Methods Mol. Biol.* **161**, 109–120 (2001). pmid: 11190499
39. L. Chang *et al.*, Herpesviral replication compartments move and coalesce at nuclear speckles to enhance export of viral late mRNA. *Proc. Natl. Acad. Sci. U.S.A.* **108**, E136–E144 (2011). doi: 10.1073/pnas.1103411108; pmid: 21555562
40. O. Kučera *et al.*, Anillin propels myosin-independent constriction of actin rings. *Nat. Commun.* **12**, 4595 (2021). doi: 10.1038/s41467-021-24474-1; pmid: 34321459
41. C. Baarlink, H. Wang, R. Grosse, Nuclear actin network assembly by formins regulates the SRF coactivator MAL. *Science* **340**, 864–867 (2013). doi: 10.1126/science.1235038; pmid: 23558171
42. Y. Nishimura *et al.*, The formin inhibitor SMIFH2 inhibits members of the myosin superfamily. *J. Cell Sci.* **134**, jcs253708 (2021). doi: 10.1242/jcs.253708; pmid: 33589498
43. D. Clift *et al.*, A Method for the Acute and Rapid Degradation of Endogenous Proteins. *Cell* **171**, 1692–1706.e18, 18 (2017). doi: 10.1016/j.cell.2017.10.033; pmid: 29153837
44. M. Murrell, P. W. Oakes, M. Lenz, M. L. Gardel, Forcing cells into shape: The mechanics of actomyosin contractility. *Nat. Rev. Mol. Cell Biol.* **16**, 486–498 (2015). doi: 10.1038/nrm4012; pmid: 26130009
45. W. Brieher, Mechanisms of actin disassembly. *Mol. Biol. Cell* **24**, 2299–2302 (2013). doi: 10.1091/mbc.e12-09-0694; pmid: 23900650
46. J. C. Sandquist, M. E. Larson, S. Woolner, Z. Ding, W. M. Bement, An interaction between myosin-10 and the cell cycle regulator Wee1 links spindle dynamics to mitotic progression in epithelia. *J. Cell Biol.* **217**, 849–859 (2018). doi: 10.1083/jcb.201708072; pmid: 29321170
47. A. D. Sousa, J. S. Berg, B. W. Robertson, R. B. Meeker, R. E. Cheney, Myo10 in brain: Developmental regulation, identification of a headless isoform and dynamics in neurons. *J. Cell Sci.* **119**, 184–194 (2006). doi: 10.1242/jcs.02726; pmid: 16371656
48. P. T. Conduit, A. Wainman, J. W. Raff, Centrosome function and assembly in animal cells. *Nat. Rev. Mol. Cell Biol.* **16**, 611–624 (2015). doi: 10.1038/nrm4062; pmid: 26373263
49. G. Greenan *et al.*, Centrosome size sets mitotic spindle length in Caenorhabditis elegans embryos. *Curr. Biol.* **20**, 353–358 (2010). doi: 10.1016/j.cub.2009.12.050; pmid: 20137951
50. E. M. Rieckhoff *et al.*, Spindle Scaling Is Governed by Cell Boundary Regulation of Microtubule Nucleation. *Curr. Biol.* **30**, 4973–4983.e10 (2020). doi: 10.1016/j.cub.2020.10.093; pmid: 33217321
51. B. Hetrick, M. S. Han, L. A. Helgeson, B. J. Nolen, Small molecules CK-666 and CK-869 inhibit actin-related protein 2/3 complex by blocking an activating conformational change. *Chem. Biol.* **20**, 701–712 (2013). doi: 10.1016/j.chembiol.2013.03.019; pmid: 23623350
52. H. Wang *et al.*, Symmetry breaking in hydrodynamic forces drives meiotic spindle rotation in mammalian oocytes. *Sci. Adv.* **6**, eaaz5004 (2020). doi: 10.1126/sciadv.aaz5004; pmid: 32284983
53. F. Farina *et al.*, The centrosome is an actin-organizing centre. *Nat. Cell Biol.* **18**, 65–75 (2016). doi: 10.1038/ncb3285; pmid: 26655833
54. A. Colin, P. Singaravelu, M. Théry, L. Blanchoin, Z. Gueroui, Actin-Network Architecture Regulates Microtubule Dynamics. *Curr. Biol.* **28**, 2647–2656.e4 (2018). doi: 10.1016/j.cub.2018.06.028; pmid: 30100343
55. A. Chaigne *et al.*, F-actin mechanics control spindle centring in the mouse zygote. *Nat. Commun.* **7**, 10253 (2016). doi: 10.1038/ncomms10253; pmid: 26727405
56. I. Bennabi *et al.*, Artificially decreasing cortical tension generates aneuploidy in mouse oocytes. *Nat. Commun.* **11**, 1649 (2020). doi: 10.1038/s41467-020-15470-y; pmid: 32245998
57. J. Wu *et al.*, Microtubule nucleation from the fibrous corona by LIC1-pericentrin promotes chromosome congression. *Curr. Biol.* **33**, 912–925.e6 (2023). doi: 10.1016/j.cub.2023.01.010; pmid: 36720222
58. H. Maiato, A. M. Gomes, F. Sousa, M. Barisic, Mechanisms of Chromosome Congression during Mitosis. *Biology* **6**, 13 (2017). doi: 10.3390/biology6010013; pmid: 28218637
59. M. K. Chong, M. Rosas-Salvans, V. Tran, S. Dumont, Chromosome size-dependent polar ejection force impairs mammalian mitotic error correction. *J. Cell Biol.* **223**, e202310010 (2024). doi: 10.1083/jcb.202310010; pmid: 38727808
60. J. C. Fierro-González, M. D. White, J. C. Silva, N. Plachta, Cadherin-dependent filopodia control preimplantation embryo compaction. *Nat. Cell Biol.* **15**, 1424–1433 (2013). doi: 10.1038/ncb2875; pmid: 24270889
61. A. Jimenez, K. Friedl, C. Leterrier, About samples, giving examples: Optimized Single Molecule Localization Microscopy. *Methods* **174**, 100–114 (2020). doi: 10.1016/j.ymeth.2019.05.008; pmid: 31078795
62. A. J. R. Booth *et al.*, Contractile acto-myosin network on nuclear envelope remnants positions human chromosomes for mitosis. *eLife* **8**, e46902 (2019). doi: 10.7554/eLife.46902; pmid: 31264963
63. B. Hernandez, MATLAB code for convex hull computation, Zenodo (2025); https://doi.org/10.5281/zenodo.15164427.

ACKNOWLEDGMENTS

We thank A. Moore for valuable technical advice and the Nikon BioImaging Lab (NBIL, Cambridge, MA, USA) for help with human embryo imaging experiments. **Funding:** The mouse work was carried out in the Plachta lab supported by grants from the NIGMS (GM139970-01), NICHD (HD102013-01A1), and Wellcome Trust–HHMI (208607/Z/17/Z) to N.P. and NICHD RSDP (K12HD849-36) and ASRM to R.M.S. The human embryo work was performed in the embryology lab at Boston IVF. **Author contributions:** B.H. conceived and designed the study, performed all imaging experiments, and wrote the paper with contributions from all other authors. P.T. performed mouse embryo isolation and microinjection. X.L. performed immunoblotting. A.D.-M., R.M.S., M.B., and S.B. performed mouse work. G.A. performed human embryo work. D.S. supervised human embryo research. N.P. supervised the study. **Competing interests:** The authors declare that they have no competing interests. **Data and materials availability:** The plasmids encoding NLS-tagged actin mutants are available upon reasonable request. All data are available in the manuscript or the supplementary materials.

SUPPLEMENTARY MATERIALS

science.org/doi/10.1126/science.ads1234
Figs. S1 to S8; Movies S1 to S8; MDAR Reproducibility Checklist

Submitted 30 July 2024; resubmitted 4 February 2025; accepted 11 April 2025

10.1126/science.ads1234

Actin organizes chromosomes and microtubules to ensure mitotic fidelity in the preimplantation embryo

Blake Hernandez, Piotr Tetlak, Ana Domingo-Muelas, Hiroki Akizawa, Robin M. Skory, Goli Ardestani, Mate Biro, Xiaolei Liu, Stephanie Bissiere, Denny Sakkas, and Nicolas Plachta

Science **388** (6749), eads1234. DOI: 10.1126/science.ads1234

Editor's summary

The process of mitotic cell division is canonically orchestrated by the mitotic spindle apparatus, which is composed of microtubules. However, cells of the early mouse embryo do not contain centrosomes, the organelles responsible for efficient spindle assembly. The exact processes governing early embryonic cell divisions has therefore remained unclear. Using live-embryo imaging, Hernandez *et al*. discovered a contractile network of nuclear actin filaments that organizes chromosomes during the early phases of mitosis (see the Perspective by Bement). The authors also observed a separate actin network that regulates spindle size. These findings support the idea that actin filaments serve essential functions during mitotic cell division in early embryos. —Stella M. Hurtley